ELSEVIER

Contents lists available at ScienceDirect

ISPRS Journal of Photogrammetry and Remote Sensing

journal homepage: www.elsevier.com/locate/isprsjprs





Low-severity spruce beetle infestation mapped from high-resolution satellite imagery with a convolutional network

- S. Zwieback $^a,^b,^*$, J. Young-Robertson c , M. Robertson c , Y. Tian $^a,^d$, Q. Chang e , M. Morris a , J. White a , J. Moan f
- ^a Geophysical Institute, University of Alaska Fairbanks, Fairbanks, AK, USA
- b Department of Geosciences, University of Alaska Fairbanks, Fairbanks, AK, USA
- c Institute of Agriculture, Natural Resources and Extension, University of Alaska Fairbanks, Fairbanks, AK, USA
- d Lawrence Livermore National Laboratory, Livermore, CA, USA
- e Department of Geography, Guelph, Ontario, Canada
- f Division of Forestry and Fire Protection, Alaska Department of Natural Resources, Anchorage. AK. USA

ARTICLE INFO

Dataset link: https://zenodo.org/doi/10.5281/zenodo.10569990, https://zenodo.org/doi/10.5281/zenodo.10569975, https://zenodo.org/doi/10.5281/zenodo.8423568

Keywords: Forestry Insect outbreak Deep learning Satellite image

ABSTRACT

Extensive mortality of susceptible spruce can be caused by spruce beetles at epidemic population levels, as in the ongoing outbreak in Southcentral Alaska. Although information on outbreak extent and severity underpins forest management and research, the data products available in Alaska have substantial gaps. Widely available high-resolution satellite imagery are a promising data source for detecting beetle kill because it is possible, though challenging, to identify individual trees. However, the applicability of automated deeplearning approaches for regional-scale mapping has not been evaluated. Here, we assess a deep convolutional network for mapping dead spruce in high-resolution (~2m) satellite imagery of Southcentral Alaska. The network identified dead spruce pixels across stand characteristics, achieving an average accuracy of 95%. To upscale to the stand scale, we mitigated overestimation of dead tree pixels at elevated severity by calibration. Stand-scale areal severity, the fraction of dead spruce pixels within a stand, was mapped with an RMSE of 0.02 at 90 m scale. The estimated severity exceeded 0.05 in fewer than 4% of the landscape, and approximately 90% of dead trees pixels were found in low-severity stands. Severity was weakly associated with stand-scale Landsat reflectance changes, a clear relation between SWIR reflectance change and severity only emerging above 0.1 severity. In conclusion, high-resolution satellite imagery are suited to automated mapping of beetle-associated kill at tree and stand scale across the severity spectrum. Such data products support forest and fire management and further understanding of the dynamics and consequences of beetle outbreaks.

1. Introduction

The spruce beetle (SB; *Dendroctonus rufipennis*) is the tree-killing insect that inflicts the greatest damage in Alaskan forests (Werner et al., 2006). The most recent, ongoing outbreak in Southcentral Alaska has affected ~2 million acres since 2016 (Fettig et al., 2022). It had spread north to Cantwell and the surrounding Alaska Range by 2020 (FS-R10-FHP, 2021).

Regional mapping of infestation extent and severity is important for understanding and responding to outbreaks (Fettig et al., 2022). Existing maps have substantial gaps because operational monitoring in Alaska relies on survey flights, ground observations and manual interpretation of high-resolution imagery (FS-R10-FHP, 2021). Consequently, we lack baseline data for answering simple questions such as where and in what forest stands the majority of dead spruce are found.

Gap-free maps could elucidate the controls, drivers and consequences of the outbreak and inform mitigation (e.g., sanitation harvest) and timber resource and fire management strategies (Senf et al., 2015).

A major knowledge gap is how to automatically map bark beetle infestation of low to moderate severity. Bark beetle tree kill has been mapped with moderate-resolution imagery such as Landsat outside Alaska (Kennedy et al., 2012; Hart and Veblen, 2015; Senf et al., 2015; Hais et al., 2016), but with poorer accuracy in low-severity stands (Meddens et al., 2013; Rodman et al., 2021; Ye et al., 2021). Conversely, very-high-resolution (<50 cm) drone imagery can resolve individual dead trees, facilitating their identification through manual image interpretation or deep convolutional neural networks across the severity spectrum (Safonova et al., 2019; Minařík et al., 2021; Kapil

^{*} Corresponding author at: Geophysical Institute, University of Alaska Fairbanks, Fairbanks, AK, USA. E-mail address: szwieback@alaska.edu (S. Zwieback).

et al., 2022). In high-resolution (~2 m) satellite imagery, identifying individual trees is possible but more challenging (White et al., 2005; Coops et al., 2006; Immitzer and Atzberger, 2014; Brandt et al., 2020), but these data enable wide coverage and also automation through neural networks.

How accurately can convolutional networks identify dead spruce trees following a beetle outbreak from $\sim 2\,\mathrm{m}$ satellite imagery? Convolutional-network-based recognition of individual trees in $\sim 2\,\mathrm{m}$ resolution imagery is well established (Li et al., 2016; Freudenberg et al., 2019; Mubin et al., 2019), in particular in sparsely vegetated environments such as the Sahel (Flood et al., 2019; Brandt et al., 2020; Reiner et al., 2023). Identifying specific species or infested trees is more challenging, in particular in densely vegetated environments where partially overlapping tree crowns cannot be fully resolved in $\sim 2\,\mathrm{m}$ imagery (Yao et al., 2021; Lassalle et al., 2022). Kislov et al. (2021) achieved a promising performance in mapping beetle-killed conifers in predominantly dense stands, emphasizing the network's ability to distinguish dead trees from spectrally similar objects such as boulders. However, the dependence of the accuracy on the infestation severity in pure and mixed stands remains unknown.

Here, we map dead spruce across the severity spectrum in South-central Alaska from high-resolution satellite images. We train and test a convolutional neural network to identify dead spruce pixels and upscale the results to stand-scale areal severity. As moderate-resolution satellite images could shed light on this and previous outbreaks of variable severity, we quantify pre- to post-outbreak changes in stand-scale reflectance. Our specific objectives are to:

- evaluate the performance of convolutional network for identifying dead spruce pixels in high-resolution satellite imagery
- 2. determine the distribution of stand-scale areal severity derived from the tree-scale classification
- assess the association of areal severity with changes in standscale Landsat reflectance

2. Background

The spruce beetle is found in all forested regions in Alaska. Extended periods of low population levels can be interrupted by outbreaks, characterized by high beetle populations that can overcome and kill healthy trees (Berg et al., 2006; Fettig et al., 2022). In Alaska, large outbreaks have almost exclusively been recorded in Southcentral (SC) Alaska, south of the Alaska Range (Holsten and Werner, 1990). The ongoing outbreak started in SC Alaska in around 2016, moving north toward the Alaska Range (FS-R10-FHP, 2021). As of 2023, it approached the Alaskan Interior, where outbreaks have historically been smaller in size and number, with the exception of a ~200,000-acre outbreak in the 1980s (Holsten and Werner, 1990).

During Alaskan outbreaks, SB preferentially attack and kill large, mature white spruce (*Picea glauca*) or Lutz spruce (*P. × lutzii*). However, Sitka spruce (*P. sitchensis*), smaller white spruce and black spruce (*P. mariana*) are also attacked (Berg et al., 2006). SB larvae and adults consume the phloem, potentially girdling the tree and inducing carbon starvation (Werner et al., 2006). Successful colonization is conditional on SB and its symbiotic fungi's subjugation of the host's defense, the effectiveness of which varies with such factors as tree age and drought (Doak, 2004; Ott et al., 2021). The expansion of the current outbreak toward the Alaskan Interior raises questions about host tree defense and SB winter survival in a climate previously thought unconducive to large outbreaks (Holsten and Werner, 1990).

The controls on infestation severity include stand composition, tree defenses and SB population numbers. Dense, almost pure stands of large, slowly-growing hosts are most heavily affected in terms of killed trees per area and, to a lesser extent, individual tree mortality (Doak, 2004). Large trees in dense stands are thought to be more heavily attacked and less resistant to infestation (Holsten and Werner, 1990;

Werner et al., 2006), but younger trees and trees in mixed stands are also affected, particularly in large outbreaks. Tree defenses are influenced by abiotic factors such as drought or wind damage and tree factors like bark thickness and phloem chemistry (Reynolds and Holsten, 1996; Werner et al., 2006). Stand composition and host resistance impact SB population dynamics, as do meteorological conditions and SB predators and parasites (Berg et al., 2006).

Spruce beetle outbreaks modify stand composition, ecosystem services and land surface processes. The death of large spruce promotes growth of the surviving trees (Sherriff et al., 2011; Campbell et al., 2019). Changes to the understory vegetation are varied, as Matsuoka et al. (2001) reported increased abundance of shrubs in the Copper River Basin, whereas grasses increased on the Kenai Peninsula (Holsten et al., 1995). Dense grass, dead trees and associated litter can impact wildfire risk and behavior (Schulz, 1995; Hicke et al., 2012). Falling snags, changes in habitat, decreasing value of timber resources, and the aesthetic deterioration of the landscape are additional concerns for stakeholders and the public (Matsuoka et al., 2001; Berg et al., 2006). Answering open questions about post-outbreak changes in water and carbon cycling and impacts on soil temperatures also requires regional remote sensing products on outbreak severity (Brown et al., 2010; Pfeifer et al., 2011; Pugh and Small, 2012; Reed et al., 2018).

3. Materials and methods

3.1. Study area and period

Our study area is located in the Susitna Lowlands (Wahrhaftig, 1965), its east and northwest margins straddling the Talkeetna Mountains and the Alaska Range, respectively (Fig. 1a). The elevation varies from less than 200 m in the central part to more than 1500 m in the northwest (Fig. 1b). We restricted most quantitative analyses to the TBL region between Talkeetna and Byers Lake, constrained by image availability and clouds. The TBL is dominated by poorly drained lowlands in the center and areas of moderate relief at the margins.

The Subarctic climate features cold and long winters (Shulski and Wendler, 2007), with mean temperatures averaging -14 °C in January in Talkeetna. For comparison, average January temperatures on the Cook Inlet coast (Anchorage) are -8 °C, while Fairbanks in the Alaskan Interior north of the Alaska Range is colder at -22°C (Alaska Climate Research Center, 2023). In Talkeetna, the mean July temperature is 16 °C. Average rainfall totals from June through September of 350 mm are intermediate between maritime Anchorage and continental Fairbanks. The region is in the isolated permafrost zone, with greater permafrost prevalence in and north of the Alaska Range (Jorgenson et al., 2008).

Spruce-dominated forests are rare in the study area, in contrast to mixed forests, wetlands, and - at higher elevations - scrub, meadows and sparsely vegetated terrain. Terrain, substrate and drainage conditions exert the strongest apparent controls on vegetation cover (Battan, 1982), as wildfires have historically been limited in frequency and size. Forest stands dominated by white spruce are rare and small in the TBL region, preferentially occurring in floodplains and at higher elevations in the Northwest where conifer fraction exceed 0.4 (Fig. 1c; from Macander et al., 2022). The lowlands predominant in the TBL area were classified as Southern Alaska Spruce-Birch-Herb (SBH) Forests and Southern Alaska Sphagnum Bogs and Herbaceous Fens (wetlands) by Jorgenson and Meidlinger (2015). SBH forests have conifer fractions of 10%-30% according to the Macander et al. (2022) product shown in Fig. 1c, dominated by beetle-preferred white spruce. Conversely, tree and conifer cover is sparse in wetlands and largely restricted to black spruce in moderately drained positions such as the transitions to SBH forests (Jorgenson and Meidlinger, 2015).

The region has been heavily affected by the SB outbreak that started in the mid-2010s (Fettig et al., 2022). Aerial Detection and Survey (ADS) flights by the USDA Forest Service, Forest Health Protection

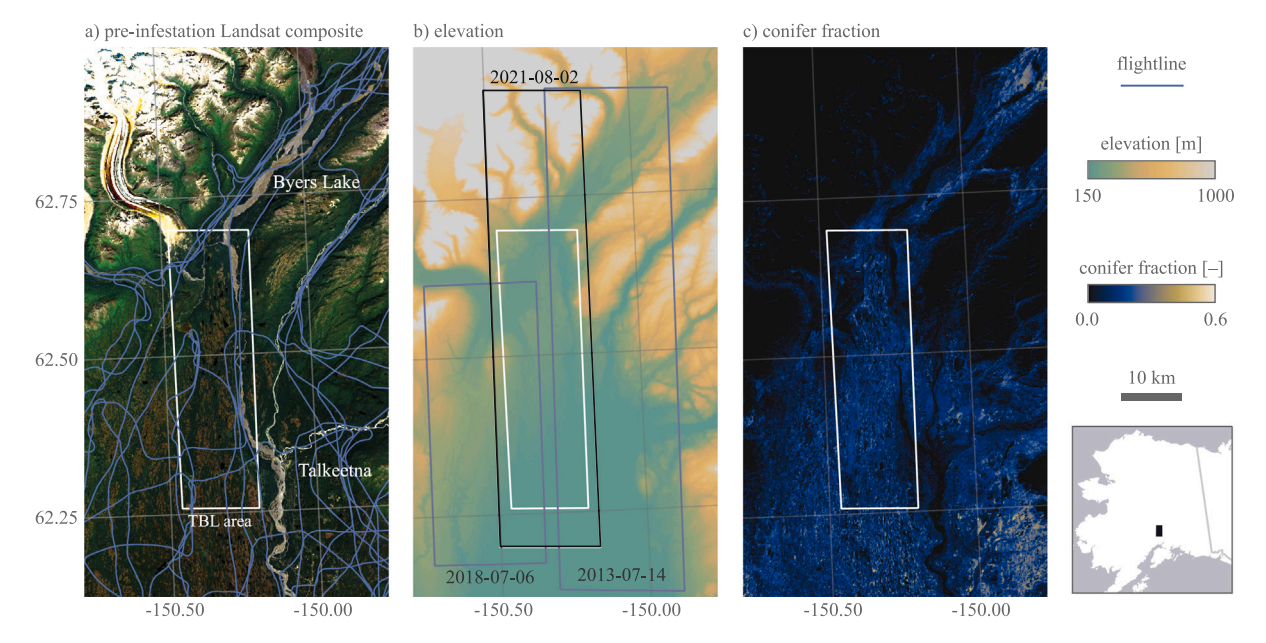


Fig. 1. The study area is centered on the Susitna Lowlands in SC Alaska, a mosaic of mixed forest and wetlands, appearing in green and brown in the 2013–2015 Landsat –8 composite (a), respectively. Aerial Detection and Survey flightlines from 2015–2019 are shown in blue. High-resolution image extent is shown in (b), along with the perimeter of the Talkeetna to Byers Lake (TBL) area. The conifer fraction in (c) from Macander et al. (2022) includes black and white spruce. (For interpretation of the references to color in this figure legend, the reader is referred to the web version of this article.)

and its partners between (2015–2019 flightlines shown in Fig. 1a) and ground observations showed the oubreak reached the TBL area within the first two years, with substantial tree mortality being noted in 2018 (FS-R10-FHP, 2018). By 2021, exhaustion of large white spruce hosts had diverted activity to smaller white spruce and also black spruce (FS-R10-FHP, 2021). Meanwhile, the outbreak has continued to move north into the Alaska Range, reaching Cantwell in approximately 2020.

3.2. O1: Tree-scale dead spruce mapping

The dead spruce we sought to identify were defoliated spruce trees, as these can be recognized on high-resolution imagery. After a lethal SB attack, the needles fade and are ultimately shed within two to three years (Werner et al., 2006). We recognize ambiguity in this definition, as death and defoliation do not coincide and partial defoliation can occur. Furthermore, attribution to SB requires external information (Wulder et al., 2009).

Dead spruce pixels were automatically identified using a deep neural network. In such a semantic segmentation task, the network takes as input a high-resolution satellite image and produces as output a pseudoprobability that a given pixel covers a dead spruce tree. To train and test the neural network, we manually delineated dead trees.

3.2.1. High-resolution imagery

We had three Maxar Worldview-2 images at our disposal (Fig. 1b). Two post-outbreak images from 2021-08-02 (1403 $\,\rm km^2)$ and 2018-07-07 (976 $\,\rm km^2)$ were complemented by one pre-outbreak image from 2013-07-14 (1930 $\,\rm km^2)$). Each image consisted of a panchromatic and a multispectral image with a posting of 0.5 and 2.0 m, respectively. We used seven multispectral bands: blue (427 nm), green (546 nm), yellow (608 nm), red (659 nm), red edge (724 nm), near infrared-1 (831 nm) and near-infrared-2 (908 nm). We omitted the coastal band due to strong atmospheric influences.

We used pansharpening to obtain a seven-band multispectral image with a spatial resolution of $\sim\!\!1.5\,\text{m}$ at a posting of 0.5 m. The Gram–Schmidt pansharpening (Aiazzi et al., 2007) took as input the panchromatic and the coarser multispectral image and replaced in each multispectral band that part that could be linearly explained by the panchromatic band with the sharper panchromatic band.

3.2.2. Training and test data

We designated 111 training areas in the pre-infestation and post-infestation image from 2013-07-14 and 2021-08-02, respectively. Each training area was $512 \,\mathrm{m} \times 512 \,\mathrm{m}$ in size, encompassing 1024^2 pixels. The areas were selected with the goal of covering a spectrum of land cover types (including areas without trees) and stand severity.

To evaluate the performance on independent data, we designated 228 test areas in the two training images (but at different locations) and in an independent image from 2018-07-16. The 2018 image was taken near the peak of the outbreak, predating the peak in mortality. The test areas were 90×90 m, the smaller size facilitating assessment of the stand-scale areal fraction estimates for objective two. The independent image enabled us to assess the transferability of the trained network to different conditions (e.g., earlier stage of infestation; different insolation and atmospheric conditions) in the same area.

Manual delineation of dead spruce trees was based on spectral, spatial and contextual clues (Coops et al., 2006; Hart and Veblen, 2015). In the visible to near-infrared spectrum, dead spruce in our study area are characterized by greater red relative to near infrared reflectance when compared to healthy white spruce (see Appendix). We predominantly relied on near-infrared-red-green composites like Fig. 2, due to the distinct teal appearance of dead spruce. Further clues of salience included: round to triangular shape; characteristic scale of ~1–8 m; triangular shadow (where free standing); in an environment where trees can grow (e.g., excluding rivers). While expert interpretation of high-resolution imagery is a standard method for assessing bark beetle damage (Coops et al., 2006; Senf et al., 2017; FS-R10-FHP, 2021), it is inherently subjective and contingent on image quality and timing (Kislov et al., 2021).

We digitized dead trees in two steps designed to ensure consistency. First, the operator (SZ, JW or MM) delineated all dead spruce in the area by drawing polygons, annotating challenging instances. These were then discussed with another person. Second, SZ reviewed and edited the area after >one week. Our goal was for each delineated polygon to comprise an individual tree crown, but two or more closely spaced individuals may be contained in a single polygon where the image resolution precluded their separation. Challenging instances mainly arose in mixed forests such as Fig. 2, where partial occlusion

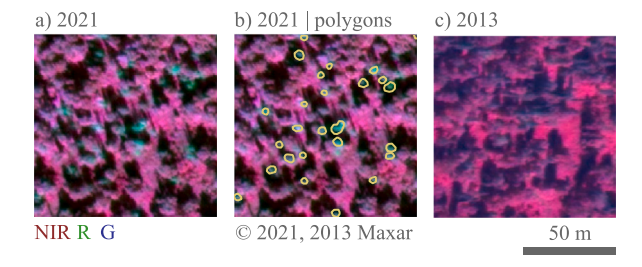


Fig. 2. Dead spruce trees have a teal appearance in false-color composites (NIR-R-G) of Worldview-2 images from Maxar. A post-infestation image (a), with manually delineated dead spruce shown in (b). No dead spruce were found in the pre-infestation image (c). (For interpretation of the references to color in this figure legend, the reader is referred to the web version of this article.)

by broadleaf trees impedes reliable identification. We did not delineate ambiguous cases of small size, predominantly in poorly drained areas where black spruce are common. The ambiguity was due to a slightly elevated visible reflectance, potentially indicating early or non-lethal infestation. The digitization yielded 9194 and 3148 dead-spruce polygons in the training and test areas, respectively.

The manually drawn polygons were rasterized for training the network. The output raster, aligned with the input raster, stored the pseudo-probability of the pixel containing dead spruce. To account for uncertainty in location of the polygons, we spatially smoothed the raster with a Gaussian filter with $\sigma=0.5\,\mathrm{m}$. To account for uncertainty in class assignment, we mixed the pseudo-probability with a uniform distribution ("label smoothing") with an admixture weight of $\alpha=10^{-3}$. This pseudo-probability raster was the target that the network was trained to replicate.

3.2.3. Training by transfer learning

The deep convolutional network for semantic segmentation is designed to incorporate complex spatial, spectral and contextual patterns such as those we relied on for manual delineation (LeCun and Bengio, 1998). We used the DeepLabV3 convolutional neural network architecture with a pre-trained Resnet50 backbone (Chen et al., 2017), as available through Pytorch. The input multichannel image is fed to the encoder, comprising the backbone and an atrous spatial pyramid pooling component for extracting multiscale information. Subsequently, the decoder produces the classification output. To account for the required characteristics of the input and output, we modified the encoder and decoder, respectively. The encoder's first layer was enlarged from three to seven bands, matching the imagery. We initialized its weights by copying those of the original layer (scaled by 0.7) (Pan et al., 2019) and disturbing them with zero-mean uncorrelated Gaussian noise, keeping the variance constant. The last layer of the decoder was replaced by a fully connected layer that yielded an output image with two bands (0: no dead spruce, 1: dead spruce), a softmax operation yielding the pseudo-probability p of dead spruce occurrence.

We trained the network by adjusting the parameters so as to minimize the misfit between the network's prediction and the manually derived labels from the training set. The initial parameter values were taken from a network that had been pre-trained for detecting objects such as bicycles on photographs from the COCO dataset (Lin et al., 2014). Our transfer learning (Pires de Lima and Marfurt, 2020) leverages the ability of the pre-trained network to extract salient visual patterns but guides it to recognize dead spruce trees in satellite images.

Training was achieved by minimizing a weighted cross entropy loss with respect to the augmented training samples (Jadon, 2020). The weight of the dead spruce class 1 was set to 20 times that of class 0 to account for class imbalance. To minimize the loss, we employed the Adam optimizer with a learning rate of 10^{-5} , batch size of eight, and 500 epochs. The data set was augmented (Shorten and Khoshgoftaar, 2019) by random cropping to 512×512 pixels (discarding three quarters of the input training image), flipping and changes in brightness and contrast for each input channel.

3.2.4. Tree-scale evaluation

To quantify the classification performance, we compared the pseudo-probability p from the convolutional network with the independent, manually derived test data across pixels. From a binary classification result based on p > 0.5, we computed the confusion matrix with respect to the test data by counting the pixels corresponding to true positives (TP; pixel contains a dead spruce and was classified as such), true negatives (TN), false negatives (FN) and false positives (FP) across all test areas. We computed three tree-scale (i.e., $0.5 \, \mathrm{m}$ m pixels) metrics; first, the overall accuracy

$$accuracy = \frac{TP + TN}{TP + TN + FP + FN}.$$
 (1)

Second, the false positive rate,

$$FPR = \frac{FP}{FP + TN},$$
 (2)

measures the fraction of pixels without dead spruce that were incorrectly classified as containing dead spruce. Third, the true positive rate,

$$TPR = \frac{TP}{TP + FN},$$
(3)

measures what fraction of pixels containing dead spruce were recognized as such by the convolutional network.

We computed these three metrics separately for (i) the same images as were used for training (2013, 2021) and (ii) for the independent image (2018).

3.3. O2: Stand-scale severity from tree-scale classification

3.3.1. Stand-scale severity

We upscaled the tree-scale binary classification to gridded areal severity estimates at the stand scale, focusing on three stand scales s between 30 and 250 m. In absence of reliable forest stand data products, we report the stand-scale results on grids with uniform sampling distance s.

Stand-scale areal severity (Hart and Veblen, 2015), \hat{f} , was estimated from the network-derived tree-scale pseudo-probability through

$$\hat{f} = \frac{1}{|\mathcal{P}_s|} \left| \left\{ m \in \mathcal{P}_s \mid p_m \ge 0.5 \right\} \right|,\tag{4}$$

where $|\cdot|$ denotes set cardinality. The set \mathcal{P}_s consists of all the 0.5 m pixels within a stand-scale pixel of size $s \times s$, and the pseudo-probability of the 0.5 m-pixel m is denoted by p_m .

The definition of areal severity differs from other common intensity metrics. The unitless \hat{f} refers to the crown area of dead trees (estimated at a scale determined by the high-resolution image) within a given area, similar to the mortality area within a grid cell computed by Meddens et al. (2013). As the denominator in Eq. (4) is the total area, \hat{f} needs to be distinguished from metrics that normalize by the treed area, the number of suitable host trees or the number of trees. For instance, the ADS intensity classification the operator assigns is based on trees with canopy fading (as opposed to needle loss) per treed area (Jason Moan, personal communication), rendering direct comparison difficult.

We obtained calibrated severity estimates \hat{f}^c from the raw severity estimate \hat{f} to compensate bias in \hat{f} at elevated severity. The calibration curve $\hat{f}^c(\hat{f})$ was established at 90 m and subsequently also applied at 30 and 250 m. Specifically, we modeled $\text{logit}(\hat{f})$, the logarithm of the odds of \hat{f} , as

$$logit(\hat{f}^{c}) = \beta_0 + \beta_1 logit(\hat{f}) + \beta_3 logit(\hat{f})^3.$$
 (5)

We estimated β , by minimizing the least-squares misfit with respect to f, the severity from the manually delineated polygons in the test areas in the training images. The constraints $\beta_1 \geq 0$ and $\beta_3 \geq 0$ were non-binding at the optimum.

We evaluated the \hat{f}^c severity estimates at 90 m using the root mean square error (RMSE) and R^2 with respect to the test data for (i) the training images and (ii) the independent image.

3.3.2. Distribution of severity across scales

We quantified the distribution of areal severity across scales $s \in \{30,90,250\,\mathrm{m}\}$ from the 2021 post-infestation image in three ways. First, we derived spatial maps. Second, we computed cumulative histograms of \hat{f}^c over \mathcal{I}_s , the set of all stands of scale s in the TBL region. Third, we evaluated the cumulative areal mortality in dependence of the areal severity f through

$$C_s(f) = \frac{1}{\sum_{n \in \mathcal{I}_s} \hat{f}_n^c} \sum_{n \in \mathcal{I}_s} \hat{f}_n^c \left[\hat{f}_n^c \le f \right], \tag{6}$$

where the Iverson bracket [q] evaluates to one when q is true and to zero otherwise. If half the dead-spruce pixels are in stands with areal severity of no more than 10%, then $C_s(0.1) = 0.5$.

3.4. O3: Spectral changes in stand-scale reflectance

3.4.1. Stand-scale spectral changes from landsat

We contrasted pre- to post-infestation Landsat spectral changes at the stand scale (30, 90, and 250 m). We opted for a simple differencing approach because of the paucity (~2/yr) of suitable Landsat images in this cloudy region. Increasing image availability favors time series approaches that account for changes on subseasonal to decadal time scales (Senf et al., 2015; Hais et al., 2016; Ye et al., 2021).

We mapped the difference Δ in shortwave infrared (SWIR) reflectance and a normalized difference index (NDI). These two quantities are proven indicators of beetle-killed trees, but including additional observables can enhance detection and attribution performance (Cohen et al., 2018). Increased SWIR reflectance is commonly used for identifying vegetation mortality (Senf et al., 2017; Zhu et al., 2020), and beetle-killed spruce show a pronounced increase in reflectance above $1.5\,\mu$ m in our study area (see Appendix). We also used a normalized index that compares the SWIR with the near infrared (NIR) reflectance,

$$NDI = \frac{SWIR - NIR}{SWIR + NIR} = -NBR,$$
(7)

exploiting the opposite direction of change in the NIR and SWIR upon tree death. It is the negative of the normalized burn ratio (NBR), historically the most popular indicator for bark beetle mapping (Kennedy et al., 2012; Senf et al., 2015).

We computed the temporal difference in the SWIR reflectance and NDI mean from Landsat by subtracting the post-outbreak (2019–2021; day of year 175–227) mean from the pre-outbreak (2014–2016) mean. The standard error was computed assuming uncorrelated errors with constant variance. For Landsat, we processed Collection 2 Level 2 images from Landsat 8 and 5 with total cloud cover of less than 15%, retaining those NIR and SWIR2 surface reflectance measurements that met the pixel-level cloud Quality Assessment (QA) based on bits 1–5. In addition to the native 30 m posting, we also evaluated the differences at 90 m and 250 m scale.

3.4.2. Association with areal severity

Kernel density estimation was used to determine the stand-scale spatial association between the spectral changes and areal severity inferred from the convolutional neural network. We computed the kernel density for (i) those pixels with more than 10% conifer fraction according to Macander et al. (2022) and (ii) all pixels in the TBL area.

4. Results

4.1. O1: Tree-scale dead spruce mapping

4.1.1. Classification results

Fig. 3 shows tree-scale classification results of eight test areas spanning a range of stand characteristics and infestation severity.

The network recognized dense white spruce across a range of areal severity (a-d). In the low-density stands in (a-b), all dead spruce were

recognized. In (b), two spruce not included in the manual delineation due to insufficient spectral contrast were identified by the network. The network also identified dead spruce in stands with greater density and severity (c–d).

The network correctly assigned low p to healthy white spruce (e), black spruce (f) and wetlands (f).

Three weaknesses are apparent in Fig. 3. First, the inflated size of dead spruce in the classification results, most pronounced in the high-severity stand (d). Second, in dense mixed forests dominated by deciduous broadleaf trees (g), the network missed dead spruce partially occluded by other trees. Third, panel (h) shows a rare example of a non-tree object that was assigned $p \gtrsim 0.5$.

4.1.2. Performance assessment

The accuracy across all test areas was 0.95. Fig. 4a shows that the network performance was almost identical for the images used during training (2021: late in outbreak; 2013: pre-outbreak) and for the 2018 image earlier in the outbreak. The accuracy decreased with the areal severity f determined from the manually delineated polygons.

The false positive rate FPR increased with severity f, exceeding 0.2 for elevated-severity stands (Fig. 4b). In the examples from Fig. 3 imaged in 2021, the false positives corresponded to the inflated size of mapped dead trees.

The true positive rate TPR was on the order of 90%, with best performance for high-severity stands. TPR was lower for stands with low and moderate severity. In the mixed forest stand of Fig. 3g imaged in 2021, the TPR was diminished because the network assigned lower p to partially occluded dead spruce.

4.2. O2: Stand-scale severity and its distribution

4.2.1. Calibration and assessment

Calibration was required for upscaling tree-scale classification results to 90 m stand-scale areal severity. The uncalibrated severity estimates \hat{f} overestimated the severity f from manual delineation in the test areas. Fig. 5a shows that \hat{f} over test areas in the same images as used for training (2013, 2021) was accurate for low $f \lesssim 0.03$ but overestimated f by more than a factor of 2 $f \gtrsim 0.1$. We corrected for this by applying the calibration curve to obtain \hat{f}^c from \hat{f} . The same curve (from the 2013 and 2021 test areas) also reduced the overestimation in the 2018 image (Fig. 5b), reducing $\hat{f} \approx 0.2$ to $\hat{f}^c \approx 0.1$ for $f \approx 0.1$.

The calibrated severity estimate \hat{f}^c achieved root-mean-square errors (RMSE) of better than 0.02 (Fig. 5c). The performance was worse at elevated severity, with RMSEs of up to 0.03.

4.2.2. Distribution of areal severity

Areal severity \hat{f}^c at the 90 and 250 m stand scale was below 0.1 in most of the TBL area in 2021 (Fig. 6a–b). Landscape fragmentation was associated with a narrower \hat{f}^c range at 250 m. Mixed-forest severity of 0.03 to 0.10 contrasts with negligible severity in wetlands, treeless floodplains and above the timberline (Fig. 6c). Stands with elevated severity $\hat{f}^c \gtrsim 0.10$ occurred at higher elevations toward the northwestern corner and also in mature floodplains.

A heterogeneous subregion shown in Fig. 6d–g contains patches with elevated severity, including a dense, almost pure stand of white spruce with $\hat{f}^c \gtrsim 0.2$ highlighted Fig. 6g. The subregion illustrates the patchy nature of \hat{f}^c in mixed forests with $0.02 \lesssim \hat{f}^c \lesssim 0.10$ and consistently low values on tree-less terrain such as floodplains (Fig. 6e).

Moderate to large areal severity locations were rare, as the cumulative histogram in Fig. 7a shows 97% of the area had severity below 0.05 at $s=90\,\mathrm{m}$ stand scale. At $s=30\,\mathrm{m}$, 70% had negligible severity $\hat{f}^\mathrm{c}<0.01$ and 6% had at least moderate severity $\hat{f}^\mathrm{c}>0.05$. At a scale of 250 m, the distribution was more narrow.

The vast majority of dead spruce trees were identified in low-severity stands (Fig. 7b). At 90 and 250 m stand scales, more than 85% of the tree-scale (0.5 m) pixels inferred to contain dead spruce were in stands with low severity $\hat{f}^c \leq 0.05$. The percentage dropped to 63 at 30 m, while 96% were in areas with $\hat{f}^c \leq 0.10$.

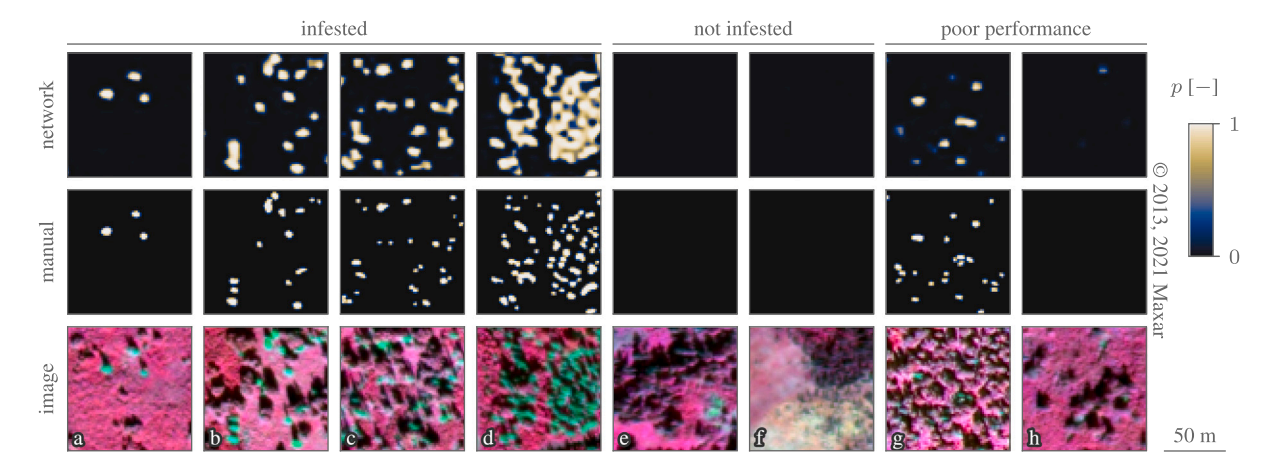


Fig. 3. The top row shows tree-scale pseudo-probabilities of dead spruce presence at 0.5 m posting, estimated by the network from 2021 (a-d, f-h) and 2013 (e) Worldview-2 images (NIR-R-G composite in bottom row). The middle row shows the probability derived from manually delineated dead spruce.

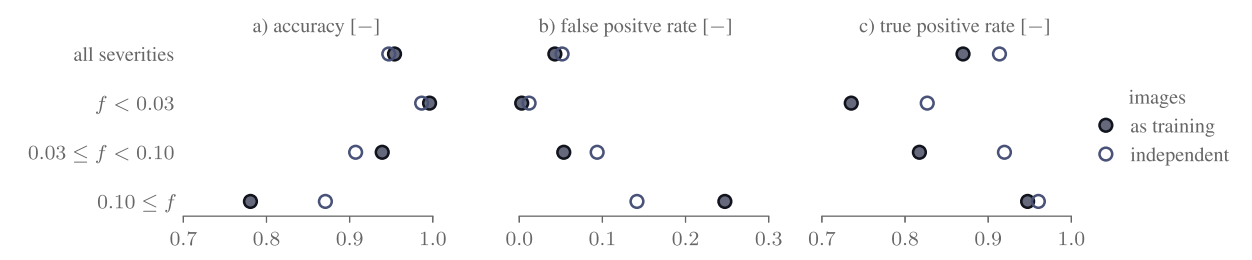


Fig. 4. Tree-scale performance metrics from comparison of network predictions with manually derived polygons over test areas. Each row shows the aggregate over a severity interval.

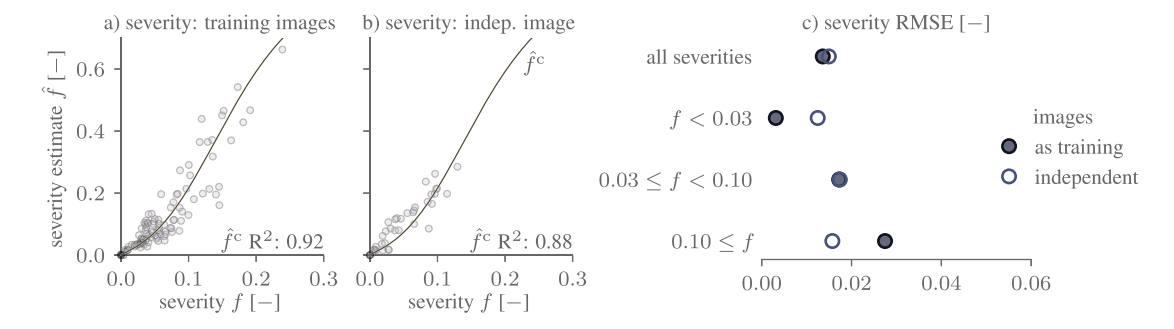


Fig. 5. Raw network-estimated areal severity \hat{f} versus areal severity derived from the manually delineated polygons within the test areas in (a) the 2013 and 2021 image, (b) the 2008 image. The curve fitted to the data in (a) converts the raw estimate \hat{f} to the calibrated areal severity \hat{f}^c . (c) RMSE of the 90 m stand-scale severity estimates \hat{f}^c relative to severity from manually delineated polygons, otherwise same as Fig. 4.

4.3. O3: Spectral changes in stand-scale reflectance

Pre- to post-outbreak spectral changes are apparent in high-severity areas. At 30 m scale, the stands identified by the network to have high severity in Fig. 6d increased in Landsat SWIR reflectance by $\gtrsim 0.03$ (Fig. 6f). Increases of ~ 0.01 were observed in mixed stands with moderate severity but also in low-severity sites dominated by black spruce or largely tree-free wetlands.

Stand-scale SWIR reflectance changes were less associated with areal severity than with wetland dynamics. Across the study area (Fig. 8a), changes in mean SWIR reflectance were dominated by wetlands, the elevated standard error in (b) reflecting strong spectral fluctuations. An association with severity at 30 and 90 m scale emerges at elevated severity $\hat{f}^c \gtrsim 0.1$ in Fig. 8d: an increase in Δ SWIR from 0.01 to 0.02 correlated with an increase in severity from 0.1 to 0.2. However, Δ SWIR alone was poor predictor of severity, especially when not excluding locations with low conifer cover such as most wetlands.

A noticeable SWIR reflectance change is only apparent in the highseverity stand in Fig. 8e. It exhibited a sustained 0.02 increase between 2017 and 2019, in contrast to low and moderate severity stands.

The association between severity and change in NDI was weaker than that with the SWIR reflectance at 30 and 90 m scale (Fig. 8d). While there was a tendency for increasing Δ NDI with increasing severity \hat{f}^c , the distribution of Δ NDI conditional on \hat{f}^c remained wide.

5. Discussion

5.1. O1: Tree-scale dead spruce mapping performance

The classification performance from $\sim 2\,\mathrm{m}$ resolution satellite imagery was deemed satisfactory in stands from low to high severity. The overall accuracy of 95% (Fig. 4) was comparable to the 94% balanced accuracy obtained by Kislov et al. (2021)'s deep network for spruce trees killed by *Ips typographus*. Across our study area, false positives in locations without dead spruce were rare, in agreement with Kislov

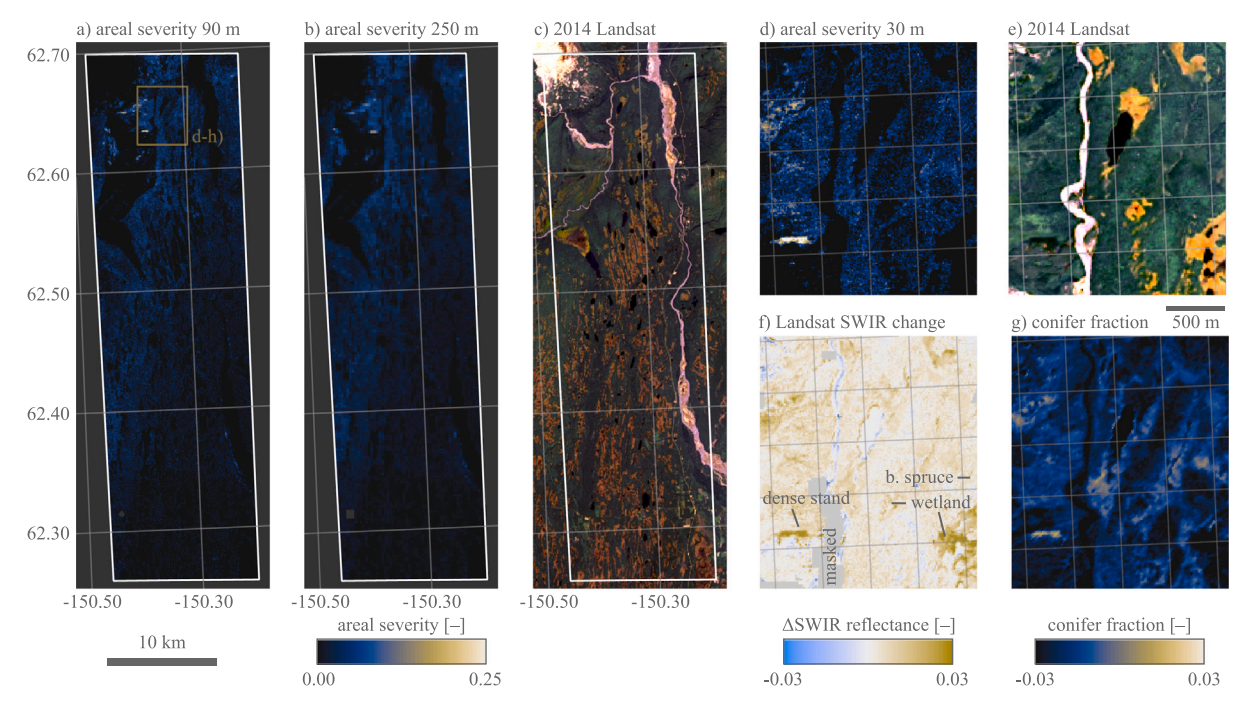


Fig. 6. (a-b) Areal severity \hat{f}^c over the TBL area at 90 and 250 m scale, respectively, and (c) a pre-infestation Landsat true-color image. Panels (d-g) show the heterogeneous subregion indicated in (a), with annotated wetlands, black [b.] spruce and a dense, high-severity white spruce stand highlighted in (f). The conifer fraction (g) is from Macander et al. (2022). (For interpretation of the references to color in this figure legend, the reader is referred to the web version of this article.)

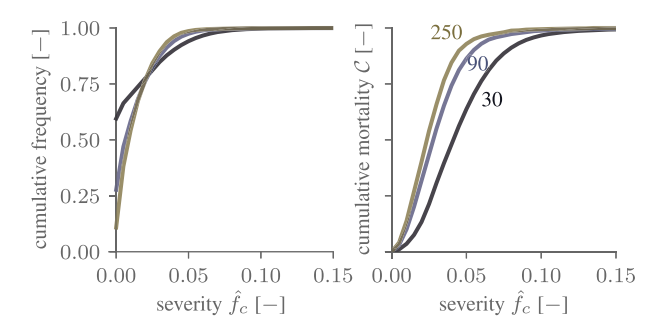


Fig. 7. (a) Cumulative distribution of areal severity \hat{f}^c across the TBL study area; (b) fraction of tree-scale dead spruce pixels in stands with below a given severity. The lines correspond to the three stand scales $s \in 30, 90, 250 \,\mathrm{m}$.

et al. (2021)'s finding that convolutional networks accurately differentiate dead spruce from spectrally similar features such as boulders. Transferability of the network, as evidenced by comparable accuracy on an independent image, can expedite operational mapping.

The principal limitations were false negatives in dense mixed forests and the inflated size in elevated-severity stands (false positives). There is a trade-off between the two types of errors, as changing, say, the loss function tends to improve one to the detriment of the other (Jadon, 2020). Future studies could benefit from improved network architectures, post-classification cleaning, and – especially in mixed forests – winter scenes or higher-resolution satellite imagery with near-nadir viewing geometries (Shrestha and Vanneschi, 2018; Brandt et al., 2020; Pires de Lima and Marfurt, 2020). At the stand scale, the calibrated upscaling compensated for the dependence of false positives and negatives on severity, achieving a severity RMSE of better than 0.02 (Fig. 5c).

Interpretation of the mapping performance needs to consider two limitations of the independent test data. First, the lack of spatially distributed ground data precludes an assessment of how accurately the training and test data captured partially or completely occluded dead spruce. Second, we were not able to directly identify a tree's species, whether it was alive or dead, or the mortality agent when

assembling the test data. Ambiguities in mixed black-spruce-dominated stands highlight the inherent ambiguities in identifying beetle-killed spruce from high-resolution imagery alone (Hart and Veblen, 2015).

5.2. O2: Most dead spruce in low-severity stands

In our study area, approximately 90% of dead spruce tree pixels were inferred in stands of low areal severity $\hat{f}^c \lesssim 0.05$ at 90 m scale. In this region with few dense stands of susceptible spruce, areal severity exceeding 0.10 was rare, such stands containing 1% of dead spruce (pixels). Conversely, stands with high SB-associated areal severity were more prevalent after an outbreak in Colorado (Hart and Veblen, 2015).

The low density of susceptible spruce hosts in mixed forests seemingly did not impede infestation. While dense stands of large white spruce have been observed to be preferentially attacked (Werner et al., 2006), Doak (2004) did not find a significant relationship between stand density and the fraction of white spruce killed by SB in the Copper River Valley in Alaska during a 1990s outbreak. Conversely, a classification tree predicting SB-induced mortality on the Kenai peninsula trained by Reynolds and Holsten (1996) identified spruce basal area relative to the total basal area and basal area of large-diameter spruce relative to spruce basal area as top-level predictors, both being positively associated with mortality. Owing to the incommensurability of field-based per-tree and remotely sensed per-area metrics such as our \hat{f}^c , development of remotely sensed estimates of the fraction of susceptible trees killed is necessary to enhance understanding of outbreak dynamics and consequences (Senf et al., 2017).

While lighter SB consequences are expected in areas of low rather than high severity (Wulder et al., 2009), the impacts on the energy and water balance, biogeochemical cycling, succession, and habitat are poorly understood in Alaska (Werner et al., 2006; Fettig et al., 2022). Safety hazards from beetle-killed trees at the Byers Lake campground in our study area further illustrate that low to moderate areal severity infestation poses a concern to the public, land managers and stakeholders (Department of Natural Resources, State of Alaska, 2019).

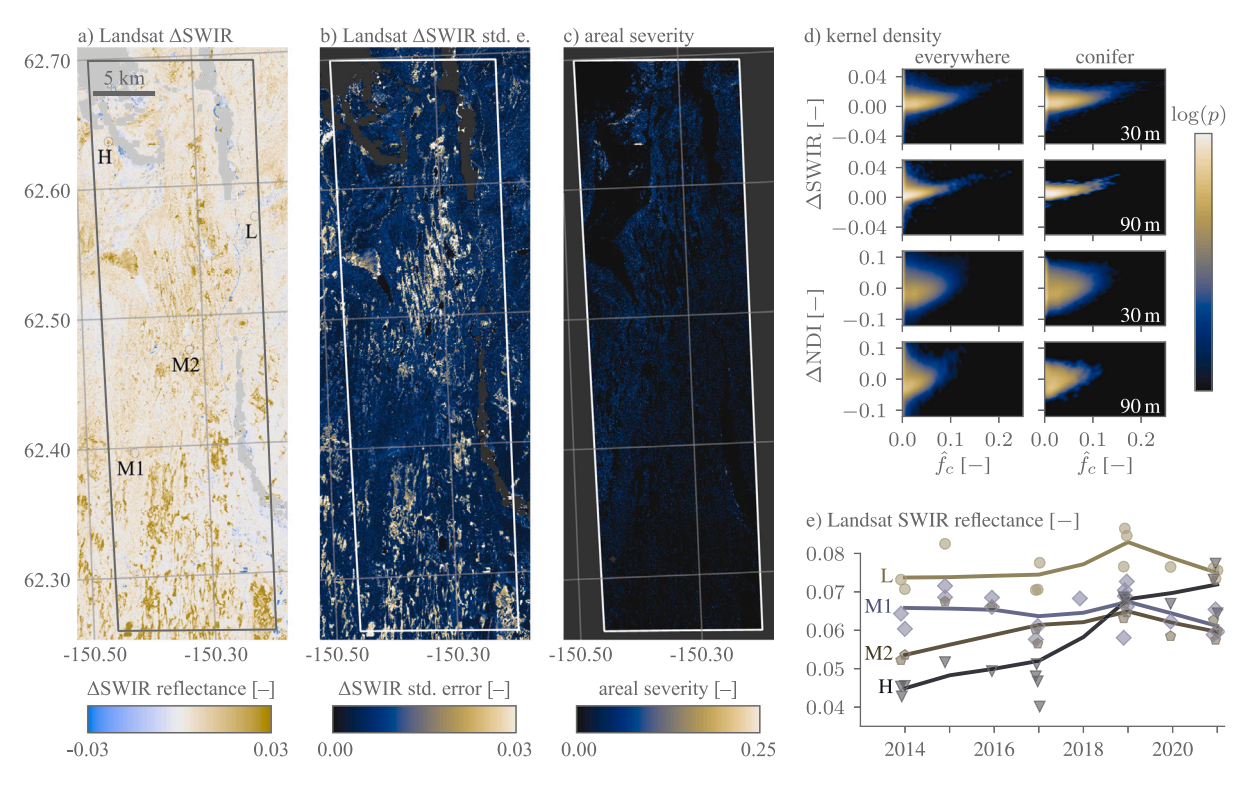


Fig. 8. Pre- to post-outbreak changes in mean Landsat SWIR reflectance (a) and associated standard error (b), alongside areal severity (c). (d) Kernel density *p* estimates of reflectance change (SWIR or NDI) and areal severity at 30 and 90 m scale (left column: all stands in TBL area, right column: only those with conifers and low standard error in the right row). (e) Timeseries of Landsat reflectance for the four stands shown in (a), L (low), M1 and M2 (moderate) and H (high) corresponding to Fig. 3a-c, respectively.

5.3. O3: Suitability of stand-scale reflectance for mapping low-severity infestation

We identified major limitations. At low to moderate areal severity, Fig. 8d shows poor association between severity and temporal changes in Landsat SWIR (reflectance and NDI), even when excluding locations with low conifer cover. Conversely, the increased SWIR reflectance in the few high-severity stands (Figs. 6f, 8e) supports the suitability of SWIR-based indices for tracking severe beetle infestations (Senf et al., 2017; Cohen et al., 2018; Zhu et al., 2020).

Mapping past and future outbreaks of low severity from Landsat alone will be challenging. The subtle reflectance changes (Fig. 8d) are compounded by data sparsity due to frequent cloud cover, curtailing time series analysis to account for subseasonal variability. In contrast to historical outbreaks, the growing availability of hyperspectral, Cubesat multispectral, thermal infrared and synthetic aperture radar hold promise for early-stage infestation and mortality mapping (Lausch et al., 2013; Immitzer and Atzberger, 2014; Einzmann et al., 2021; Zakrzewska and Kopeć, 2022). The richness and frequency of data opens opportunities for machine learning approaches (Cohen et al., 2018; Ye et al., 2021), trained with, among other data sources, independent machine learning predictions from high-resolution imagery (Kislov et al., 2021).

6. Conclusion

To map dead spruce at tree and stand scale across the severity spectrum in Southcentral Alaska, we trained, assessed and applied a convolutional neural network using satellite imagery of $\sim\!\!2\,\mathrm{m}$ resolution. Our work addressed the knowledge gap of how well convolutional networks perform on such satellite images in which individual trees are more difficult to recognize than in $\sim\!\!0.1\,\mathrm{m}$ drone images. Our principal findings are as follows.

- The network was able to identify dead spruce over variable stand characteristics and areal severity, achieving an average accuracy of 95%. Moderate weaknesses were omissions of dead spruce in dense mixed forest stands (false negatives) and the inflated extent of dead spruce (false positives) at elevated severity.
- At the 90 m stand scale, the fraction of 0.5 m pixels containing dead spruce was less than 0.05 in 97% of the study area.
 Ninety percent of the dead tree pixels were located in stands with severity below 0.05.
- Areal severity was weakly associated with temporal changes in stand-scale SWIR reflectance change derived from Landsat. A clear increase in SWIR reflectance was observed for the few stands with high severity.

Automated satellite-based insect infestation mapping in sparsely populated regions such as Alaska enables better management and response strategies and is critical for improved understanding of the dynamics and consequences of bark beetle outbreaks.

CRediT authorship contribution statement

S. Zwieback: Formal analysis, Funding acquisition, Software, Validation, Writing – original draft, Writing – review & editing. J. Young-Robertson: Funding acquisition, Project administration, Validation, Writing – review & editing. M. Robertson: Data curation, Investigation, Project administration, Writing – review & editing. Y. Tian: Data curation, Investigation. Q. Chang: Investigation, Writing – review & editing. M. Morris: Investigation. J. White: Investigation. J. Moan: Conceptualization, Resources, Validation, Writing – review & editing.

Declaration of competing interest

The authors declare that they have no known competing financial interests or personal relationships that could have appeared to influence the work reported in this paper.

Data availability

The manually delineated dead spruce tree outlines for training and test data have been uploaded to https://zenodo.org/doi/10.5281/zenodo.10569990, the PyTorch model to https://zenodo.org/doi/10.5281/zenodo.10569975, and the severity maps to https://zenodo.org/doi/10.5281/zenodo.8423568. The high-resolution Maxar imagery are proprietary.

Acknowledgments

This work utilized data made available through the NASA Commercial Smallsat Data Acquisition (CSDA) Program. Maxar data were provided by the Commercial Archive Data for NASA investigators (cad4nasa.gsfc.nasa.gov) under the National Geospatial-Intelligence Agency's NextView license agreement. Landsat-8 Collection 2 Tier 1 Level 2 data were accessed through Google Earth Engine. This work was supported by the National Aeronautics and Space Administration (NASA), USA under Grants 80NSSC19K1494 and 80NSSC22M0046 (Alaska NASA EPSCoR Program), by the National Science Foundation (NSF), USA under Grant OIA-1753748, and the United States Department of Agriculture (USDA) under Grant ALK22-03. Dar Roberts and Junjie Liu are thanked for guidance on field spectroscopy and carbon cycling, respectively.

Appendix. Shoot-scale spectra of healthy and dead spruce

To characterize spectral differences between healthy and dead white spruce, we collected shoot-scale field spectra using a PSR+ 3500 Field Spectroradiometer. The reflectance factor as a function of wavelength was determined by dividing the raw shoot-scale observations obtained using the fiber-optic probe (without lens, 10 cm distance) by white spectralon reference measurements. Data were acquired north of the TBL study region in July 2022.

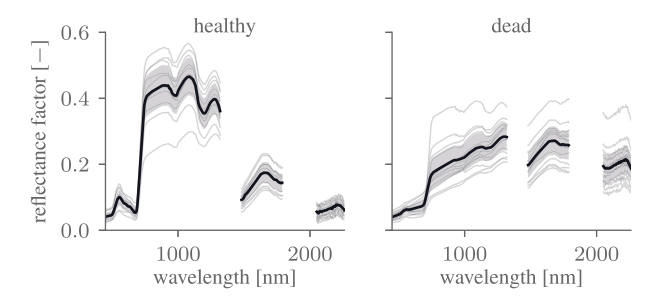


Fig. A.9. Field spectra of health and beetle-infested dead white spruce. The dark line shows the grand mean, the shaded area the mean absolute deviation, and the faint line the individual scans.

Fig. A.9 compares the reflectance spectra for healthy (no signs of infestation) and dead (needles shed; signs of SB infestation). The clearest differences for dead versus healthy trees are the weakening of the green peak and red edge (residual red edge from understory vegetation?); decreased reflectance in the near-infrared; increased reflectance in the shortwave infrared; and weaker water absorption features.

References

- Aiazzi, B., Baronti, S., Selva, M., 2007. Improving component substitution pansharpening through multivariate regression of MS + Pan data. IEEE Trans. Geosci. Remote Sens. 45 (10), 3230–3239.
- Alaska Climate Research Center, 2023. Temperature Normals. URL: https://akclimate. org/.
- Battan, A.R., 1982. A Literature Survey on the Wetland Vegetation of Alaska. U.S. Army Engineer Waterways Experiment Station.

- Berg, E.E., David Henry, J., Fastie, C.L., De Volder, A.D., Matsuoka, S.M., 2006. Spruce beetle outbreaks on the Kenai Peninsula, Alaska, and Kluane National Park and Reserve, Yukon Territory: Relationship to summer temperatures and regional differences in disturbance regimes. Forest Ecol. Manag. 227 (3), 219–232. http://dx.doi.org/10.1016/j.foreco.2006.02.038.
- Brandt, M., Tucker, C.J., Kariryaa, A., Rasmussen, K., Abel, C., Small, J., Chave, J., Rasmussen, L.V., Hiernaux, P., Diouf, A.A., et al., 2020. An unexpectedly large count of trees in the West African Sahara and Sahel. Nature 587 (7832), 78–82.
- Brown, M., Black, T., Nesic, Z., Foord, V., Spittlehouse, D., Fredeen, A., Grant, N., Burton, P., Trofymow, J., 2010. Impact of mountain pine beetle on the net ecosystem production of lodgepole pine stands in British Columbia. Agricult. Forest Meteorol. 150 (2), 254–264.
- Campbell, E.M., Antos, J.A., vanAkker, L., 2019. Resilience of southern Yukon boreal forests to spruce beetle outbreaks. Forest Ecol. Manag. 433, 52–63. http://dx.doi. org/10.1016/j.foreco.2018.10.037.
- Chen, L., Papandreou, G., Schroff, F., Adam, H., 2017. Rethinking atrous convolution for semantic image segmentation. CoRR abs/1706.05587. arXiv:1706.05587.
- Cohen, W.B., Yang, Z., Healey, S.P., Kennedy, R.E., Gorelick, N., 2018. A LandTrendr multispectral ensemble for forest disturbance detection. Remote Sens. Environ. 205, 131–140. http://dx.doi.org/10.1016/j.rse.2017.11.015.
- Coops, N.C., Johnson, M., Wulder, M.A., White, J.C., 2006. Assessment of QuickBird high spatial resolution imagery to detect red attack damage due to mountain pine beetle infestation. Remote Sens. Environ. 103 (1), 67–80.
- Department of Natural Resources, State of Alaska, 2019. Two state campgrounds closed due to bark beetle-infested trees. Press release. URL: www.dnr.alaska.gov.
- Doak, P., 2004. The impact of tree and stand characteristics on spruce beetle (Coleoptera: Scolytidae) induced mortality of white spruce in the Copper River Basin, Alaska. Can. J. Forest Res. 34 (4), 810–816. http://dx.doi.org/10.1139/x03-256
- Einzmann, K., Atzberger, C., Pinnel, N., Glas, C., Böck, S., Seitz, R., Immitzer, M., 2021. Early detection of spruce vitality loss with hyperspectral data: Results of an experimental study in Bavaria, Germany. Remote Sens. Environ. 266, 112676. http://dx.doi.org/10.1016/j.rse.2021.112676.
- Fettig, C.J., Asaro, C., Nowak, J.T., Dodds, K.J., Gandhi, K.J.K., Moan, J.E., Robert, J., 2022. Trends in bark beetle impacts in North America during a period (2000–2020) of rapid environmental change. J. Forestry 120 (6), 693–713. http://dx.doi.org/10. 1093/iofore/fyac021.
- Flood, N., Watson, F., Collett, L., 2019. Using a U-net convolutional neural network to map woody vegetation extent from high resolution satellite imagery across Queensland, Australia. Int. J. Appl. Earth Obs. Geoinf. 82, 101897.
- Freudenberg, M., Nölke, N., Agostini, A., Urban, K., Wörgötter, F., Kleinn, C., 2019.
 Large scale palm tree detection in high resolution satellite images using U-Net.
 Remote Sens. 11 (3), http://dx.doi.org/10.3390/rs11030312.
- FS-R10-FHP, 2018. Forest Health Conditions in Alaska 2018. Technical Report R10-PR-44, U.S. Forest Service, Alaska Region.
- FS-R10-FHP, 2021. Forest Health Conditions in Alaska 2021. Technical Report FS-R10-FHP Publication R10-PR-47, U.S. Department of Agriculture, Forest Service, Alaska Region.
- Hais, M., Wild, J., Berec, L., Bruna, J., Kennedy, R., Braaten, J., Brož, Z., 2016. Landsat imagery spectral trajectories—important variables for spatially predicting the risks of bark beetle disturbance. Remote Sens. 8 (8), 687.
- Hart, S.J., Veblen, T.T., 2015. Detection of spruce beetle-induced tree mortality using high- and medium-resolution remotely sensed imagery. Remote Sens. Environ. 168, 134–145. http://dx.doi.org/10.1016/j.rse.2015.06.015, URL: https://www.sciencedirect.com/science/article/pii/S0034425715300456.
- Hicke, J.A., Johnson, M.C., Hayes, J.L., Preisler, H.K., 2012. Effects of bark beetlecaused tree mortality on wildfire. Forest Ecol. Manag. 271, 81–90. http://dx.doi. org/10.1016/j.foreco.2012.02.005.
- Holsten, E.H., Werner, R.A., 1990. Comparison of white, Sitka, and Lutz spruce as hosts of the spruce beetle in Alaska. Can. J. Forest Res. 20 (3), 292–297. http://dx.doi.org/10.1139/x90-043.
- Holsten, E.H., Werner, R.A., Develice, R.L., 1995. Effects of a spruce beetle (Coleoptera: Scolytidae) outbreak and fire on Lutz spruce in Alaska. Environ. Entomol. 24 (6), 1539–1547. http://dx.doi.org/10.1093/ee/24.6.1539.
- Immitzer, M., Atzberger, C., 2014. Early detection of bark beetle infestation in Norway spruce (Picea abies, L.) using WorldView-2 data. Photogramm. Fernerkund. Geoinf. 5, 351–367.
- Jadon, S., 2020. A survey of loss functions for semantic segmentation. In: 2020 IEEE Conference on Computational Intelligence in Bioinformatics and Computational Biology. CIBCB, pp. 1–7. http://dx.doi.org/10.1109/CIBCB48159.2020.9277638.
- Jorgenson, T., Meidlinger, D., 2015. The Alaska Yukon Region of the Circumboreal Vegetation Map (CBVM). Technical Report, Conservation of Arctic Flora and Fauna (CAFF)..
- Jorgenson, M., Yoshikawa, K., Kanevskiy, M., Shur, Y., Romanovsky, V., Marchenko, S., Grosse, G., Brown, J., Jones, B., 2008. Permafrost characteristics of Alaska. In: Proceedings of the Ninth International Conference on Permafrost. University of Alaska: Fairbanks, pp. 121–122.
- Kapil, R., Marvasti-Zadeh, S.M., Goodsman, D., Ray, N., Erbilgin, N., 2022. Classification of bark beetle-induced forest tree mortality using deep learning. arXiv preprint arXiv:2207.07241.
- Kennedy, R.E., Yang, Z., Cohen, W.B., Pfaff, E., Braaten, J., Nelson, P., 2012. Spatial and temporal patterns of forest disturbance and regrowth within the area of the Northwest Forest Plan. Remote Sens. Environ. 122, 117–133.

- Kislov, D.E., Korznikov, K.A., Altman, J., Vozmishcheva, A.S., Krestov, P.V., 2021. Extending deep learning approaches for forest disturbance segmentation on very high-resolution satellite images. Remote Sens. Ecol. Conserv. 7 (3), 355–368. http://dx.doi.org/10.1002/rse2.194.
- Lassalle, G., Ferreira, M.P., La Rosa, L.E.C., de Souza Filho, C.R., 2022. Deep learning-based individual tree crown delineation in mangrove forests using very-high-resolution satellite imagery. ISPRS J. Photogramm. Remote Sens. 189, 220–235. http://dx.doi.org/10.1016/j.isprsjprs.2022.05.002, URL: https://www.sciencedirect.com/science/article/pii/S0924271622001411.
- Lausch, A., Heurich, M., Gordalla, D., Dobner, H.-J., Gwillym-Margianto, S., Salbach, C., 2013. Forecasting potential bark beetle outbreaks based on spruce forest vitality using hyperspectral remote-sensing techniques at different scales. Forest Ecol. Manag. 308, 76–89. http://dx.doi.org/10.1016/j.foreco.2013.07.043.
- LeCun, Y., Bengio, Y., 1998. Convolutional networks for images, speech, and time series. In: The Handbook of Brain Theory and Neural Networks. MIT Press, Cambridge, MA, USA, pp. 255–258. http://dx.doi.org/10.5555/303568.303704.
- Li, W., Fu, H., Yu, L., Cracknell, A., 2016. Deep learning based oil palm tree detection and counting for high-resolution remote sensing images. Remote Sens. 9 (1), 22.
- Lin, T.-Y., Maire, M., Belongie, S., Hays, J., Perona, P., Ramanan, D., Dollár, P., Zitnick, C.L., 2014. Microsoft COCO: Common objects in context. In: Computer Vision–ECCV 2014: 13th European Conference, Zurich, Switzerland, September 6-12, 2014, Proceedings, Part V 13. Springer, pp. 740–755.
- Macander, M.J., Nelson, P.R., Nawrocki, T.W., Frost, G.V., Orndahl, K.M., Palm, E.C., Wells, A.F., Goetz, S.J., 2022. Time-series maps reveal widespread change in plant functional type cover across Arctic and boreal Alaska and Yukon. Environ. Res. Lett. 17 (5), 054042.
- Matsuoka, S.M., Handel, C.M., Ruthrauff, D.R., 2001. Densities of breeding birds and changes in vegetation in an Alaskan boreal forest following a massive disturbance by spruce beetles. Can. J. Zool. 79 (9), 1678–1690.
- Meddens, A.J., Hicke, J.A., Vierling, L.A., Hudak, A.T., 2013. Evaluating methods to detect bark beetle-caused tree mortality using single-date and multi-date Landsat imagery. Remote Sens. Environ. 132, 49–58. http://dx.doi.org/10.1016/j.rse.2013. 01.002.
- Minařík, R., Langhammer, J., Lendzioch, T., 2021. Detection of bark beetle disturbance at tree level using UAS multispectral imagery and deep learning. Remote Sens. 13 (23), 4768.
- Mubin, N.A., Nadarajoo, E., Shafri, H.Z.M., Hamedianfar, A., 2019. Young and mature oil palm tree detection and counting using convolutional neural network deep learning method. Int. J. Remote Sens. 40 (19), 7500–7515.
- Ott, D.S., Davis, T.S., Mercado, J.E., 2021. Interspecific variation in spruce constitutive and induced defenses in response to a bark beetle-fungal symbiont provides insight into traits associated with resistance. Tree Physiol. 41 (7), 1109–1121. http://dx.doi.org/10.1093/treephys/tpaa170.
- Pan, B., Shi, Z., Xu, X., Shi, T., Zhang, N., Zhu, X., 2019. CoinNet: Copy initialization network for multispectral imagery semantic segmentation. IEEE Geosci. Remote Sens. Lett. 16 (5), 816–820. http://dx.doi.org/10.1109/LGRS.2018.2880756.
- Pfeifer, E.M., Hicke, J.A., Meddens, A.J., 2011. Observations and modeling of above-ground tree carbon stocks and fluxes following a bark beetle outbreak in the western United States. Global Change Biol. 17 (1), 339–350. http://dx.doi.org/10.1111/j.1365-2486.2010.02226.x.
- Pires de Lima, R., Marfurt, K., 2020. Convolutional neural network for remote-sensing scene classification: Transfer learning analysis. Remote Sens. 12 (1), http://dx.doi. org/10.3390/rs12010086.
- Pugh, E., Small, E., 2012. The impact of pine beetle infestation on snow accumulation and melt in the headwaters of the Colorado River. Ecohydrology 5 (4), 467–477.
- Reed, D.E., Ewers, B.E., Pendall, E., Frank, J., Kelly, R., 2018. Bark beetle-induced tree mortality alters stand energy budgets due to water budget changes. Theor. Appl. Climatol. 131, 153–165.

- Reiner, F., Brandt, M., Tong, X., Skole, D., Kariryaa, A., Ciais, P., Davies, A., Hiernaux, P., Chave, J., Mugabowindekwe, M., et al., 2023. More than one quarter of Africa's tree cover is found outside areas previously classified as forest. Nature Commun. 14 (1), 2258.
- Reynolds, K.M., Holsten, E.H., 1996. Classification of spruce beetle hazard in Lutz and Sitka spruce stands on the Kenai Peninsula, Alaska. Forest Ecol. Manag. 84 (1–3), 251–262.
- Rodman, K.C., Andrus, R.A., Veblen, T.T., Hart, S.J., 2021. Disturbance detection in Landsat time series is influenced by tree mortality agent and severity, not by prior disturbance. Remote Sens. Environ. 254, 112244.
- Safonova, A., Tabik, S., Alcaraz-Segura, D., Rubtsov, A., Maglinets, Y., Herrera, F., 2019.

 Detection of fir trees (Abies sibirica) damaged by the bark beetle in unmanned aerial vehicle images with deep learning. Remote Sens. 11 (6), 643.
- Schulz, B., 1995. Changes Over Time in Fuel-Loading Associated with Spruce Beetle-Impacted Stands of the Kenai Peninsula, Alaska. Technical Report Technical Report R10-TP-53, USDA Forest Service, Forest Health Management.
- Senf, C., Pflugmacher, D., Wulder, M.A., Hostert, P., 2015. Characterizing spectral-temporal patterns of defoliator and bark beetle disturbances using Landsat time series. Remote Sens. Environ. 170, 166–177. http://dx.doi.org/10.1016/j.rse.2015.09.019
- Senf, C., Seidl, R., Hostert, P., 2017. Remote sensing of forest insect disturbances: Current state and future directions. Int. J. Appl. Earth Obs. Geoinf. 60, 49-60.
- Sherriff, R.L., Berg, E.E., Miller, A.E., 2011. Climate variability and spruce beetle (Dendroctonus rufipennis) outbreaks in south-central and southwest Alaska. Ecology 92 (7), 1459–1470. http://dx.doi.org/10.1890/10-1118.1, arXiv:https://esajournals.onlinelibrary.wiley.com/doi/pdf/10.1890/10-1118.1.
- Shorten, C., Khoshgoftaar, T.M., 2019. A survey on image data augmentation for deep learning. J. Big Data 6 (1), 1–48.
- Shrestha, S., Vanneschi, L., 2018. Improved fully convolutional network with conditional random fields for building extraction. Remote Sens. 10 (7), 1135.
- Shulski, M., Wendler, G., 2007. The Climate of Alaska. University of Alaska Press.
- Wahrhaftig, C., 1965. Physiographic divisions of Alaska. In: Geological Survey Professional Paper 482. US Government Printing Office, Washington, DC.
- Werner, R.A., Holsten, E.H., Matsuoka, S.M., Burnside, R.E., 2006. Spruce beetles and forest ecosystems in south-central Alaska: A review of 30 years of research. Forest Ecol. Manag. 227 (3), 195–206. http://dx.doi.org/10.1016/j.foreco.2006.02.050.
- White, J.C., Wulder, M.A., Brooks, D., Reich, R., Wheate, R.D., 2005. Detection of red attack stage mountain pine beetle infestation with high spatial resolution satellite imagery. Remote Sens. Environ. 96 (3), 340–351. http://dx.doi.org/10.1016/j.rse. 2005.03.007.
- Wulder, M.A., White, J.C., Grills, D., Nelson, T., Coops, N.C., Ebata, T., 2009. Aerial overview survey of the mountain pine beetle epidemic in British Columbia: Communication of impacts. J. Ecosyst. Manag..
- Yao, L., Liu, T., Qin, J., Lu, N., Zhou, C., 2021. Tree counting with high spatial-resolution satellite imagery based on deep neural networks. Ecol. Indic. 125, 107591. http://dx.doi.org/10.1016/j.ecolind.2021.107591.
- Ye, S., Rogan, J., Zhu, Z., Hawbaker, T.J., Hart, S.J., Andrus, R.A., Meddens, A.J.H., Hicke, J.A., Eastman, J.R., Kulakowski, D., 2021. Detecting subtle change from dense Landsat time series: Case studies of mountain pine beetle and spruce beetle disturbance. Remote Sens. Environ. 263, 112560. http://dx.doi.org/10.1016/j.rse. 2021.112560.
- Zakrzewska, A., Kopeć, D., 2022. Remote sensing of bark beetle damage in Norway spruce individual tree canopies using thermal infrared and airborne laser scanning data fusion. For. Ecosyst. 9, 100068.
- Zhu, Z., Zhang, J., Yang, Z., Aljaddani, A.H., Cohen, W.B., Qiu, S., Zhou, C., 2020. Continuous monitoring of land disturbance based on Landsat time series. Remote Sens. Environ. 238, 111116. http://dx.doi.org/10.1016/j.rse.2019.03.009.